A Variational Correction Method as an Alternative to Forced Rejection of Sidelobe-Contaminated Bistatic Doppler Measurements

MICHEL CHONG AND NABIL LAMRANI

Laboratoire d'Aérologie, CNRS, and Université de Toulouse, Toulouse, France

MARTIN HAGEN

Intitut für Physik der Atmosphäre, DLR, Oberpfaffenhofen, Wessling, Germany

ABSTRACT

The problem of sidelobe contamination of bistatic apparent Doppler velocity measurements involved in a bistatic Doppler radar network is examined. So far in the context of 3D wind field analysis, by combining a traditional Doppler radar with one or more bistatic receivers, identification and hence removal of regions of high degrees of contamination were necessarily crucial steps to obtaining reliable wind fields. This study proposes an alternative solution to the forced rejection of bistatic Doppler data suspected to be contaminated by sidelobe echoes, on the basis of restoring the nonmeasured "actual" (i.e., noncontaminated) bistatic Doppler velocity from both monostatic radar and bistatic receiver measurements. The correction method is based on a modeled expression of the observed bistatic apparent Doppler velocity defined as the reflectivity-weighted average of actual Doppler velocity of particles within individual volume samples, including the antenna gain pattern of both transmitting and receiving radars. The searched actual Doppler velocity is a solution of an underdetermined inverse problem that can be handled as a constrained linear inversion problem, through a variational least squares analysis method.

The performances of the proposed method are analyzed, using simulated radar observations involving one remote receiver. An example of application to experimental data collected by the Deutsches Zentrum für Luft und Raumfahrt (DLR) bistatic Doppler radar network within a moderate precipitation system observed on 8 May 2000 in Germany is also presented. Pseudo-Doppler observations of a tropical squall-line system are used to quantify the effective improvement of the correction method on the bistatic Doppler velocity and hence the retrieved 3D wind field. Statistics of the differences are presented between observed and idealized (sidelobe free) velocity structures on the one hand, and corrected and idealized velocity structures on the other hand. Clearly shown is the very low level of the corrected minus idealized differences (mean and standard deviation) against the significantly high level of the observed minus idealized differences. As previously observed, maximum correction occurs in regions of potentially high gradients of reflectivity. It is also found that regions of low observed minus idealized differences remain unchanged after correction, which means that the sidelobe-correction method only acts on needed regions and does not introduce any artificial modification.

1. Introduction

Wurman et al. (1993) first introduced the concepts of bistatic multiple-Doppler weather radar networks and data analysis so as to deduce two- and three-dimensional wind fields. Compared to traditional (common transmitter–receiver antenna, so-called monostatic) multiple-Doppler radar systems, a bistatic Doppler radar network only requires one traditional transmitting radar associated with one or more passive, nontransmitting radar receivers with a low-gain antenna, easily installed at remote sites around it. Therefore, the bistatic receivers offer the possibility of having one or more additional and simultaneous reflectivity and Doppler measurements of precipitation targets illuminated by the incident radiation emitted by the transmitting radar and scattered obliquely toward each receiver. Because of their extremely low cost (less than one-

thirtieth to one-fiftieth of an additional transmitter, as mentioned in Wurman et al. 1993; Protat and Zawadzki 1999), bistatic receivers can be viewed as an economic alternative to several Doppler radar systems designed for the determination of the three-dimensional wind field. For this purpose, Wurman et al. (1993), Wurman (1994), Protat and Zawadzki (1999), Takaya and Naka-zato (2002), Satoh and Wurman (2003), and Friedrich and Hagen (2004a,b) have investigated the reliability of wind estimation by combining a traditional Doppler radar with one (dual-Doppler analysis) or more (multiple-Doppler analysis) bistatic receivers in experimental (simulation) or operational conditions.

Although these authors showed that bistatic Doppler systems can provide realistic wind fields, a critical exploration of potential sources of errors in the bistatic measurements is necessary to discard them prior to the wind analysis. As pointed out by Wurman et al. (1993), one of the drawbacks to such networks lies in the non-scanning low-gain antenna of the receiver. In particular, its wide viewing angle (typically 50°–60° in the horizontal and 10°–20° in the vertical) can yield nonnegligible sidelobe and secondary scattering contamination from the transmitting radar antenna. In most situations, the contamination levels are acceptable, and Wurman et al. (1993) suggested reducing them by the use of higher-gain receiving antennas at the cost of reducing the volume visible to each receiver. So far, a lot of attention has been given to methods to eliminate data area with a high degree of contamination. Previous observations clearly showed that echo regions with large gradients of reflectivity heavily degrade the quality of both bistatic reflectivity and Doppler velocity measurements (e.g., de Elía and Zawadzki 2000; Friedrich and Hagen 2004a).

Using a sidelobe simulation model, de Elía and Zawadzki (2000) estimated a contamination index to detect areas of low-quality data. They defined it as the ratio between simulated sidelobe and total powers that reach the receiver, from the reflectivity measured by the monostatic radar. The method presented by Satoh and Wurman (2003) is similar to that of the previous authors but consists of comparing the measured bistatic reflectivity and a "clean" bistatic radar reflectivity, which is derived from the measured transmitting radar reflectivity and a bistatic radar equation. A constant threshold in the reflectivity difference is used as an elimination criterion of data with larger differences. Friedrich and Hagen (2004a) developed a quality-control scheme including, notably, another form of the contamination index based on the observed gradient of the monostatic radar reflectivity. In any case, identification and hence removal of regions with strong con-tamination can lead to a serious reduction of the area of available bistatic measurements, which is detrimental in the context of dual- or multiple-Doppler analysis. Moreover, the excluded zone may quite contain important dynamic features. Although it is possible that the use of multiple bistatic receivers can be a solution in limiting its spatial extension, the problem of side-lobe contamination remains (de Elía and Zawadzki 2000).

The objective of this paper is to propose a method to correct for the contribution of sidelobe effects to the measurements of bistatic Doppler velocity, as an alternative to the forced rejection of contaminated Doppler data. It is based on the measured transmitting radar reflectivity and the antenna gain of both transmitting and receiving radars, which are used to model the measured bistatic Doppler velocity in terms of "actual" bistatic Doppler velocity. In essence, the modeled velocity is derived from the expression of the reflectivity-weighted average of actual Doppler velocity of particles within the sampled volume (Doviak and Zrnić 1993). This can be viewed as an inverse problem that will be solved using a variational least squares adjustment technique. The formalism of this inverse problem and its numerical solution are presented in section 2. Simulations of the reflectivity and Doppler observations from a transmitting radar and one bistatic receiver are used in section 3 to evaluate the performances of the proposed method. Synthetic radar samplings will be obtained within a squall-line system, as simulated by a nonhydrostatic cloud-resolving model. Comparisons will be made of the bistatic Doppler velocity before and after the sidelobe correction with an idealized velocity that would result from an ideal sidelobe-free transmitting radar (say, its antenna gain pattern is represented by a pure Dirac function). The corresponding Cartesian wind fields that result from an application of the multiple-Doppler synthesis and continuity adjustment technique (MUSCAT) by Bousquet and Chong (1998) will also be analyzed to complete this comparative study. Finally, section 4 gives an example of application to a real case observed on 8 May 2000, by the bistatic Doppler radar network at the Deutsches Zentrum für Luft und Raumfahrt (DLR) at Oberpfaffenhofen near Munich in southern Germany.

2. Correcting for the sidelobe contamination of bistatic Doppler radar measurements

The various above-cited works on bistatic Doppler systems widely describe the theoretical framework and, particularly, the basic equations for the bistatic geom-
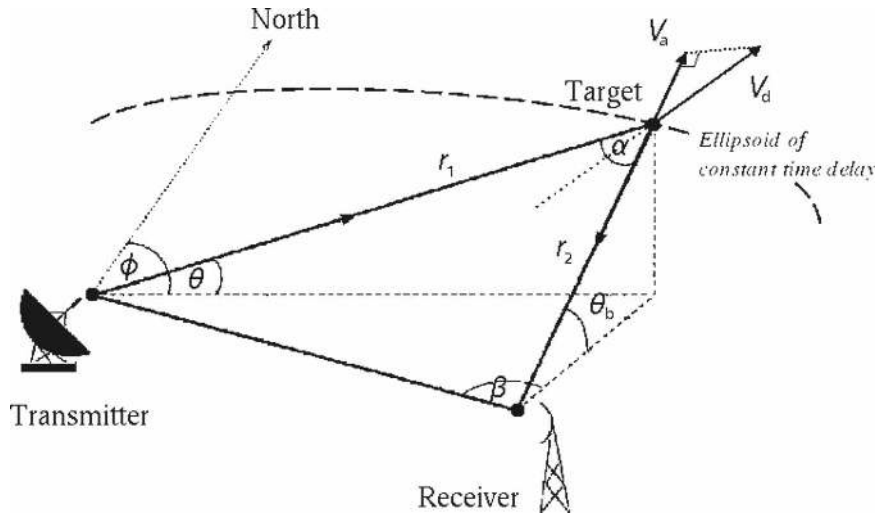
FIG. 1. Schematic representation of the geometry of a bistatic Doppler radar network. See text for the definition of the various variables. Adapted from de Elía and Zawadzki (2000).

etry and bistatic Doppler velocity. In this section, the conceptual description will not be detailed. Moreover, because the formalism of the proposed method is based on the sidelobe description of de Elía and Zawadzki (2000), their notations of the various parameters used to characterize a measurement (e.g., time delay, angular positioning, bistatic angle, apparent measured bistatic velocity versus bistatic Doppler velocity) are adopted to give some consistency with their study. The main geometrical definitions in the bistatic geometry are recalled in Fig. 1.

a. The inverse problem of bistatic Doppler observations

In Doppler measurements, only displacements of particles that are illuminated by incident radiation and that change the distance (path length) of the transmitter–target–receiver between two successive pulses should be considered. Targets located on surfaces of equal distance or constant delay time give return signals (backscattered signal for a monostatic radar, obliquely scattered for a remote receiver) with the same phase. Therefore, only particles' motions that are perpendicular to these surfaces can be detected. Such surfaces of equal distance are spheres centered at the transmitter in the case of monostatic measurements, with radially oriented Doppler velocity. They are described by ellipsoids with positions of both transmitter and receiver as foci in the case of bistatic measurements, and Doppler velocity is perpendicular to them, that is, along a line that bisects the transmitter–target–receiver angle,

so-called bistatic angle. By construction, the measured bistatic velocity along the receiver–target path, so-called apparent velocity, is defined as the projection of the bistatic Doppler velocity onto the receiver–target line, with a geometry-dependent projection angle (see Fig. 1).

As shown by de Elía and Zawadzki (2000), the sidelobe contamination of reflectivity measurements is determined by the two-way transmitting antenna pattern in the monostatic system, while it can be approximated by the one-way transmitting pattern in a bistatic radar system, mainly because of the broad azimuthal pattern of the bistatic receiver. As a consequence, the sidelobe effects (dB) for the bistatic receiver are twice as intense. Because the measured Doppler velocity is a reflectivity-weighted average of contributing targets' motions, the same conclusion can be applied to the sidelobe contamination of Doppler measurements. The state-of-the-art monostatic radars have significantly reduced sidelobe errors, but they are not totally error free. However, because their one-way transmitting antenna gain may have first sidelobes at typically -30 to -35 dB, the monostatic measurements can be assumed as sidelobe-error free, while this is not the case for the bistatic measurements.

According to Doviak and Zrnić (1993) and following the same development as in de Elía and Zawadzki (2000) to simulate the reflectivity [their Eq. (14)], the measured bistatic Doppler velocity expressed as the integrated contribution of scatterers inside this illuminated volume, including sidelobe radiation and located on an ellipsoid of constant delay time, may be written as

$$\overline{v_a}(r_1, \phi, \theta) = \frac{\int v_a(r_1', \phi', \theta') \, Z(r_1', \phi', \theta') \, I(r_2', \phi', \theta') \, d\phi' \, d\theta'}{\int Z(r_1', \phi', \theta') \, I(r_2', \phi', \theta') \, d\phi' \, d\theta'} \,, \tag{1}$$

where Z (mm^6 m^{-3}) is the monostatic radar reflectivity, v_a is the apparent Doppler velocity along the receiver-target direction, r_1 and r_2 (primed or not) are the transmitter-target and target-receiver distances, respectively, and ϕ and θ (primed or not) are the monostatic azimuth and elevation pointing angles, respectively. Primed variables ϕ' and θ' in Eq. (1) are the integration variables that sweep the entire ellipsoid, and they correspond to well-defined transmitter-target and target-receiver distances $r_1'(\phi', \theta')$ and $r_2'(\phi', \theta')$. The I is a gain-weighting function defined as

$$I(r_2', \phi', \theta') = \frac{G_t(\phi' - \phi, \theta' - \theta) G_r(\beta', \theta_b') \cos^2\gamma \cos\theta'}{r_2'^2 \cos^2(\alpha'/2)} \,, \tag{2}$$

where G_t and G_r are the transmitter and bistatic receiver antenna gain, respectively, β and θ_b are the receiver-target pointing angles with respect to the transmitter-receiver baseline and the horizontal, respectively (see Fig. 1), α is the bistatic (transmitter-target-receiver) angle, and γ defines the angle formed by the polarization vectors of the scattered signal and the receiver (see Fig. C1 in de Elía and Zawadzki 2000). As in Eq. (1), primed α, β, and θ_b in Eq. (2) are also functions of the integration variables (ϕ', θ').

Note that v_a in the integrand of Eq. (1) reflects the unknown actual bistatic apparent velocity at the considered target location (r_1', ϕ', θ'), while the resulting integration $\overline{v_a}$ is the measured apparent velocity assumed to be originated from scatters illuminated by the main lobe at (r_1, ϕ, θ). Defining $\omega = ZI/\int ZI \, d\phi' \, d\theta'$ as the normalized weighting function, Eq. (1) can be simply written as

$$\overline{v_a}(r_1, \phi, \theta) = \int v_a(r_1', \phi', \theta') \omega(r_1', r_2', \phi', \theta') \, d\phi' \, d\theta'. \tag{3}$$

Taking into account the discrete data sampling in azimuth and elevation and the limited sidelobe contribution around the pointing angle (direction of the principal axis of the radar antenna gain pattern), the unknown actual v_a can be considered as a solution of an inverse problem that could be obtained using a linear regularization method (Press et al. 1992), hereafter presented.

b. A variational least squares inverse solution

In essence, bistatic data sampling closely follows the monostatic radar sampling along a radial, with regular prescribed time delays. Because successive conical scans are performed with a regular azimuthal increment at each specified elevation, both bistatic and monostatic data are available in a discrete polar grid. Therefore, Eq. (3) can be discretized onto these (ϕ, θ) grid points on each ellipsoid of constant delay time or total distance $r_1 + r_2$. With the transmitter antenna having gain levels that rapidly decrease from the main lobes with first sidelobe of a few degrees, it is quite natural to limit the integration in Eq. (3) to those points that are illuminated by the main lobe and first sidelobe. Moreover, due to the noncoincidence of monostatic and bistatic data along a radial, observed monostatic reflectivity on spheres should be interpolated beforehand onto bistatic ellipsoids to evaluate the normalized weighting function [Eq. (2)]. Radial linear interpolation is performed from two successive monostatic data points on either side of a bistatic observation. If j and k represent the grid indices on an ellipsoid along ϕ and θ, respectively, then the measured apparent velocity $\overline{v_a}$ at (j, k) can be finally approximated as

$$\overline{v_a}(\varphi_j, \theta_k) = \sum_{k'} \sum_{j'} \omega(\varphi_{j'}, \theta_{k'}) v_a(\varphi_{j'}, \theta_{k'}) \Delta\varphi \Delta\theta,$$

$$\equiv \sum_{k'} \sum_{j'} \omega'(\varphi_{j'}, \theta_{k'}) v_a(\varphi_{j'}, \theta_{k'}), \tag{4}$$

where summations involve all grid points that are illuminated by both antennas. The range of j' and k' is dependent on the radar scan and the considered angular aperture of the transmitting radar. With an antenna rotation of 1° in azimuth and elevation angles, and an axisymmetric representation of the antenna pattern over 4° about the main axis, j' and k' extend over four grid points on either side of j and k.

With respect to the unknown variables v_a, the set of Eq. (4) represents an underdetermined system of linear equations, which can be inverted by using a constrained linear inversion method. In this study, the variational least squares analysis is expressed as a solution of minimizing the following functional J expressed at discrete grid points:

$$J = \sum_k \sum_j J_1(\phi_j, \theta_k) + \mu \sum_q \sum_p J_2(\phi_p, \theta_q), \quad \text{with} \tag{5}$$

$$J_1(\phi_j, \theta_k) = \left[\sum_{k'} \sum_{j'} \omega'(\phi_{j'}, \theta_{k'}) v_a(\phi_{j'}, \theta_{k'}) - \overline{v_a}(\phi_j, \theta_k) \right]^2,$$

$$J_2(\phi_p, \theta_q) = \left[\left(\frac{\partial^2 v_a}{\partial \phi^2} \right)^2 + \left(\frac{\partial^2 v_a}{\partial \theta^2} \right)^2 + 2 \left(\frac{\partial^2 v_a}{\partial \phi \partial \theta} \right)^2 \right]_{\phi_p, \theta_q} \Delta\phi\Delta\theta.$$

Indices p and q stand for only grid points, where J_2 can be evaluated, which implies the existence of retrieved v_a. The J_1 is the adjustment of v_a to the measured apparent velocity $\overline{v_a}$ over the domain of observed data, while J_2, the regularization term that acts as a low-pass filter, is evaluated according to a finite difference scheme (Testud and Chong 1983). The coefficient μ is a relative weight between data adjustment and constraint terms, including implicitly the normalization factor for the units of these terms. Ideally, the solution in v_a would consist of obtaining zero for the integrated value of the adjustment term J_1. However, because of the inherent numerical approximations in the discrete form of Eq. (5) and the errors attached to the measurements, a tolerance should be considered. In this study, an iterative search of the optimal μ is performed, which leads to a final integrated value of J_1 equal to about 15% of an initial value computed by considering the observed apparent velocity as an initial solution. The minimization of J [Eq. (5)] and the optimal μ are repeatedly performed for each bistatic ellipsoid.

3. Performances of the correction method

a. Antenna characteristics and numerical datasets

To evaluate the correction method, simulated radar observations (Doppler velocity and reflectivity) from a bistatic radar network with only one bistatic receiver are used hereafter. The antenna characteristics are those of the DLR bistatic Doppler radar network, which consists of the monostatic C-band polarimetric diversity Doppler radar (POLDIRAD; Schroth et al. 1988) and three bistatic receivers with horizontal and vertical angular apertures of 60° and 8°, respectively. Two of them are equipped with a second antennas of 22° vertical aperture designed for thunderstorm observation and this type of antenna is considered in this study. The one-way antenna gain patterns of the transmitting radar and remote bistatic receiver are shown in Figs. 2, 3, respectively. The sidelobe level of the monostatic radar (Fig. 2a) is lower than −32 dB, while the low gain of the receiver (Fig. 3a) ranges roughly between −5 and −20 dB. A discretized form is introduced

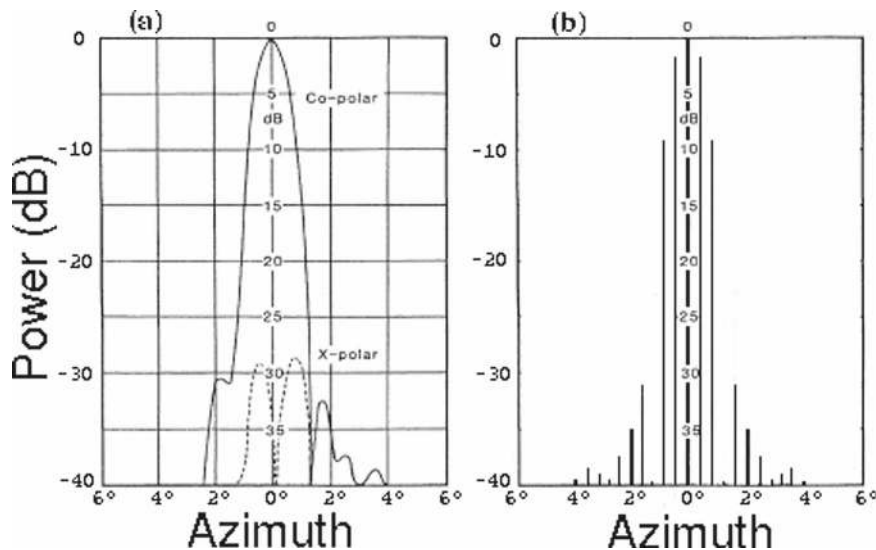
FIG. 2. One-way antenna pattern (dB) of the DLR monostatic radar (POLDIRAD) within 6° azimuthal span: (a) measured pattern and (b) axisymmetric discrete pattern. Adapted from Friedrich (2002).
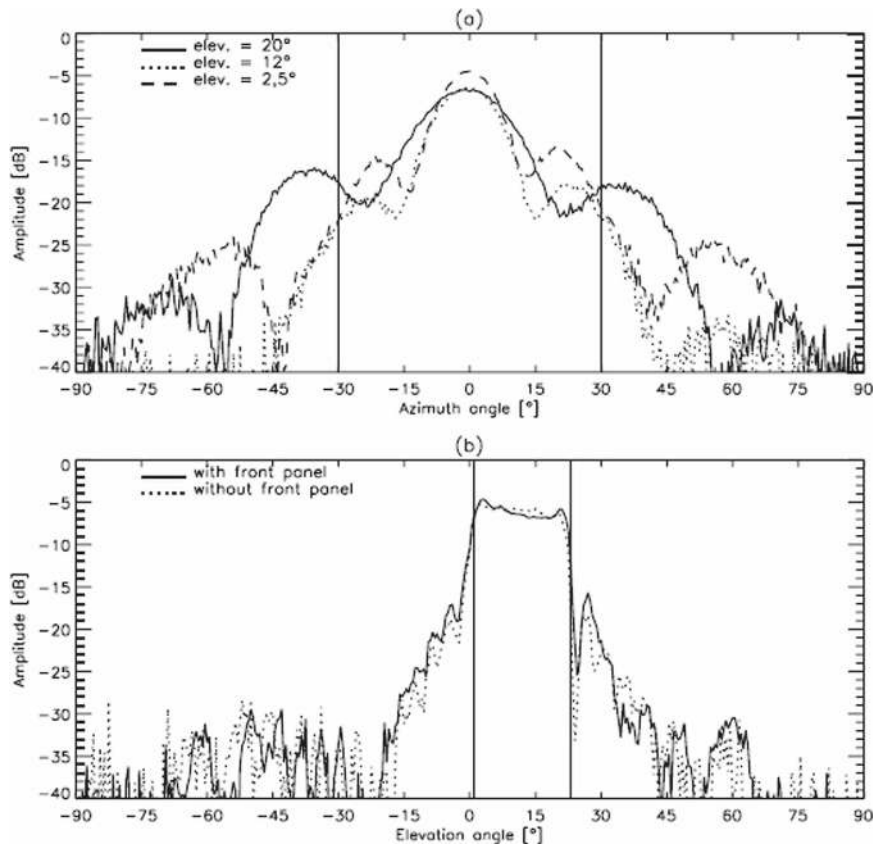
FIG. 3. One-way receiving power pattern (dB) of the vertically polarized bistatic antenna measured in (a) azimuthal direction and for 2.5°, 12°, and 20° elevation angles and (b) vertical direction for an azimuth angle of 0°, with (solid line) and without (dashed line) front panel. Adapted from Friedrich (2002).

in the simulated sampling and numerical code of the correction method. Figure 2b depicts the discrete one-way antenna gain of the monostatic radar every 0.4° up to 4°, and it is assumed to be axisymmetric about the principal axis. The receiver's antenna pattern is discretized (not shown) every 2° in the horizontal (azimuthal) direction over the full 60° (30° on either side of the principal axis) span at the considered elevation in Fig. 3a. These discrete gain values are used to interpolate the antenna gain at any specific azimuth and elevation viewing angles of the observed radar bins, from both the monostatic radar and the bistatic receiver. Because the bistatic reflectivity is not used in the correction method, only the monostatic radar reflectivity will be sampled (simulated) along with monostatic and apparent bistatic Doppler velocity. Sampled monostatic reflectivity is defined as the two-way gain-weighted average of particles' reflectivity illuminated by the monostatic radar beam at the discretizing angle resolution of 0.4° in both the azimuth and the elevation about the principal axis. For Doppler velocity, Eq. (3) is used with

the gain-weighting function I defined in Eq. (2) for the bistatic apparent velocity, while an equivalent equation with $I(r_1', \phi', \theta') = G_t^2(\phi' - \phi, \theta' - \theta) \cos\theta'/r_1'^2$ can be found for the monostatic radial velocity.

The radar samplings are derived from the three-dimensional wind and reflectivity fields associated with an African squall-line system, as simulated by the mesoscale nonhydrostatic (Meso-NH) atmospheric model, jointly developed by the Centre National de Recherches Météorologiques and Laboratoire d'Aérologie (Lafore et al. 1998) over a domain of 350 km × 400 km with a grid resolution of 2.5 km × 2.5 km. A variable vertical resolution is considered, ranging from 150 m near the surface to 700 m at the top level of 15 km. Linear distance interpolation from the closest model grid values is used to specify the wind components and reflectivity at an observation point. Figure 4a presents a horizontal section of the wind vectors and reflectivity contours at 0.5-km altitude within a restricted domain of 60 km × 60 km (this is the Doppler analysis domain used in the following). It shows the middle portion of a northwest-
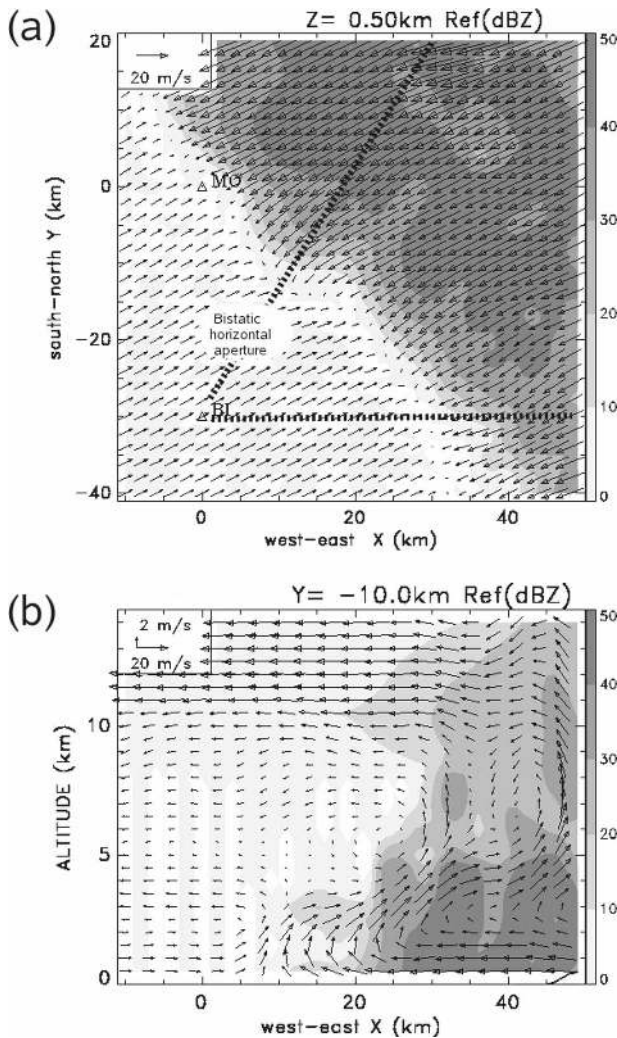
FIG. 4. (a) Wind vectors and reflectivity (dBZ) pattern (gray-scale) at 0.5-km altitude within a squall-line system as simulated by the Meso-NH model. Winds are plotted every 2 km, and the scale is indicated in the top left corner. Positions of the monostatic radar (labeled MO) and bistatic receiver (BI), from which pseudo-Doppler observations are performed, are reported. (b) Vertical west–east cross section of wind vectors and reflectivity at $y = -10$ km.

elongated (300-km long) squall line with well-defined opposing front-to-rear flow (southwest region) and rear-to-front flow (northeast region), which is associated with reflectivity >40 dBZ. Origin of the Cartesian frame (with x pointing to east and y toward north) coincides with the position of the monostatic (MO) radar, while the bistatic (BI) receiver is located 30 km to the south, as reported in Fig. 4a. Figure 4b shows a vertical cross section at $y = -10$ km, which indicates the vertical extension of the convective cells (>30 dBZ) ranging from 5- to 12-km altitude. The flow structure is composed of marked low-level rear-to-front flow behind

low-to-mid front-to-rear flow feeding convective updrafts that detrain at upper levels into a forward anvil. The orientation of the receiver (principal axis) is toward 60° from north, and its angular aperture can capture major features of the squall-line system, as can be seen in Fig. 4a. Radar sampling is over a range of 60 km with a range resolution of 300 m (i.e., 200 range gates). Due to the depth of the squall-line system (14 km), a series of 18 conical scans with an azimuthal resolution of 1° is performed at the respective elevations of 0.5°, 1.0°, 1.5°, 2.0°, 2.5°, 3.0°, 3.5°, 4.0°, 5.0°, 6.0°, 7.5°, 9.0°, 10.5°, 12.0°, 13.5°, 15.0°, 17.0° and 20.0°. As for the bistatic sampling, 200 gates are also considered with a delay time increment of 2 μs, corresponding to a variation of 600 m in the transmitter-target-receiver path length.

Two datasets have been generated. The first one uses the discretized radar beam patterns (including sidelobes), and it is referred to as the "observed" dataset to which the variational correction method applies. The second one is an "idealized" (error free) dataset because it is derived by representing the antenna gain as a pure Dirac function (i.e., without main lobe extension and sidelobes), which is of course impractical in current applications. Here, it only provides a means for quantifying the degree of the sidelobe contamination and correction through a comparative study between idealized and observed data on the one hand, and idealized and corrected data on the other hand. This terminology will be used hereafter.

b. Sidelobe effects and correction

Examples of the bistatic apparent Doppler velocity before and after sidelobe correction, along with the idealized velocity, are given in Fig. 5 for two different scan elevation angles of the transmitting radar (0.5° and 9°, respectively). Data are represented in the radar polar grid. In this section and the next, positive Doppler velocity is defined toward the receiver. At both low (top) and high (bottom) elevation angles, we can note how sidelobe contamination may greatly affect the apparent Doppler velocities in some areas when comparing idealized (left) and observed (middle) measurements. This occurs to the east of the radar at a low elevation (20 m s^{-1} contour) and to the east of the receiver at a higher elevation (–10 m s^{-1} contour). On the contrary, details of an idealized Doppler velocity field are mostly recovered when sidelobe correction (right) is implemented.

As noted by de Elía and Zawadzki (2000), regions of high reflectivity and well illuminated by both antennas will predominate, consistent with the Doppler velocity–
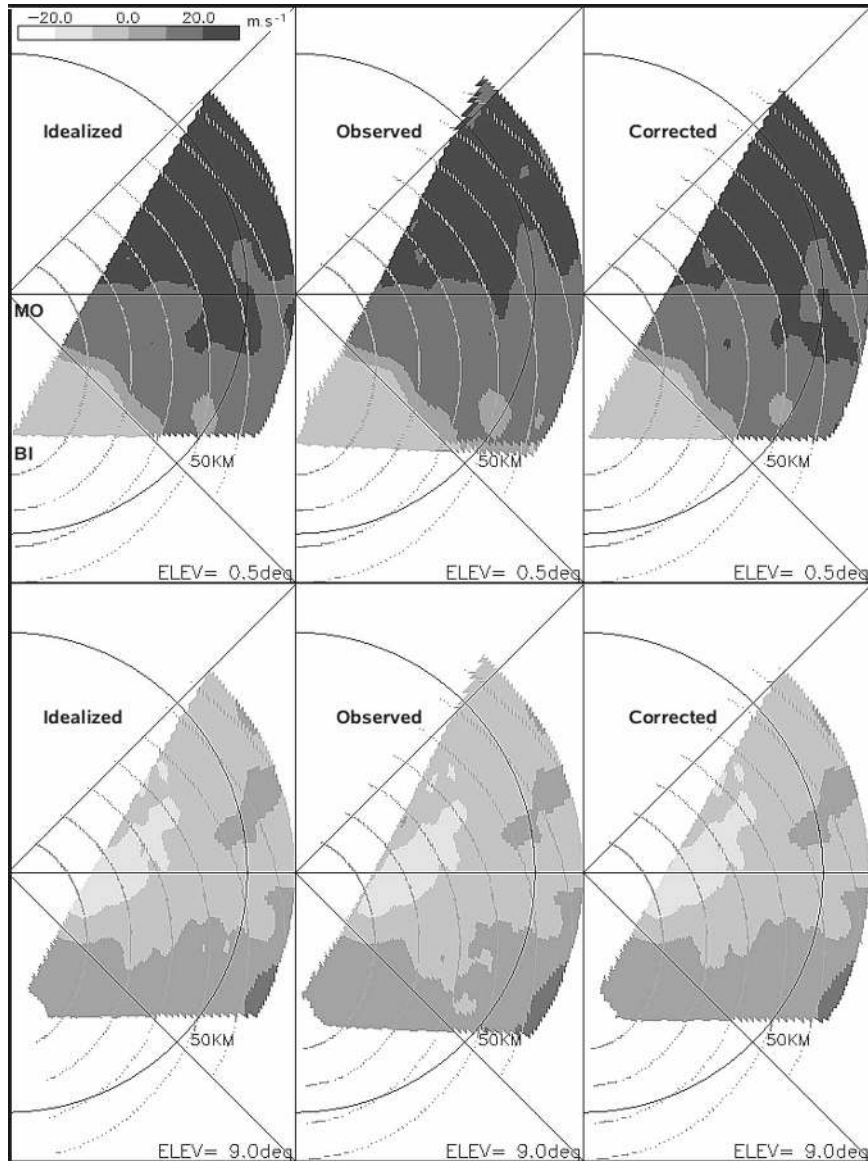
FIG. 5. PPI representation at (top) 0.5° and (bottom) 9° elevation angles of (left) idealized (no sidelobes), (middle) observed (sidelobes included), and (right) sidelobe-corrected bistatic apparent Doppler velocity (m s^{-1}), respectively, in the polar grid of the monostatic radar. Bistatic receiver is located 30 km to the south of the transmitting radar, having an antenna aperture of 60° and oriented (principal axis) toward 60°. Ellipsoids of constant time delay corresponding to total path lengths of 45, 60, 75, . . . km are plotted. Datasets are issued from a radar sampling of a simulated tropical squall line.

weighting function ω in Eq. (3). Because noncontaminated bistatic Doppler velocity changes with viewpoint, the observed ω-weighted velocity is then highly dependent on its distribution with respect to the ω function shape within the region illuminated. In particular, the presence of high-velocity shear may contribute to the exacerbation of the Doppler velocity contamination. Figure 5 shows that the contamination at a low elevation angle occurs at 40–50-km range from MO radar in

regions where reflectivity varies between 40 and 50 dBZ and horizontal flow presents a vertical shear (Fig. 4b). No contamination is observed along the squall-line leading edge with reflectivity of 0–30 dBZ over less than 10 km. At a higher elevation angle, the Doppler velocity contamination is found along this leading edge where the marked horizontal gradients of reflectivity may extend up to 5–8-km altitude. It occurs at a distance (30–50 km from MO) where the range-increasing
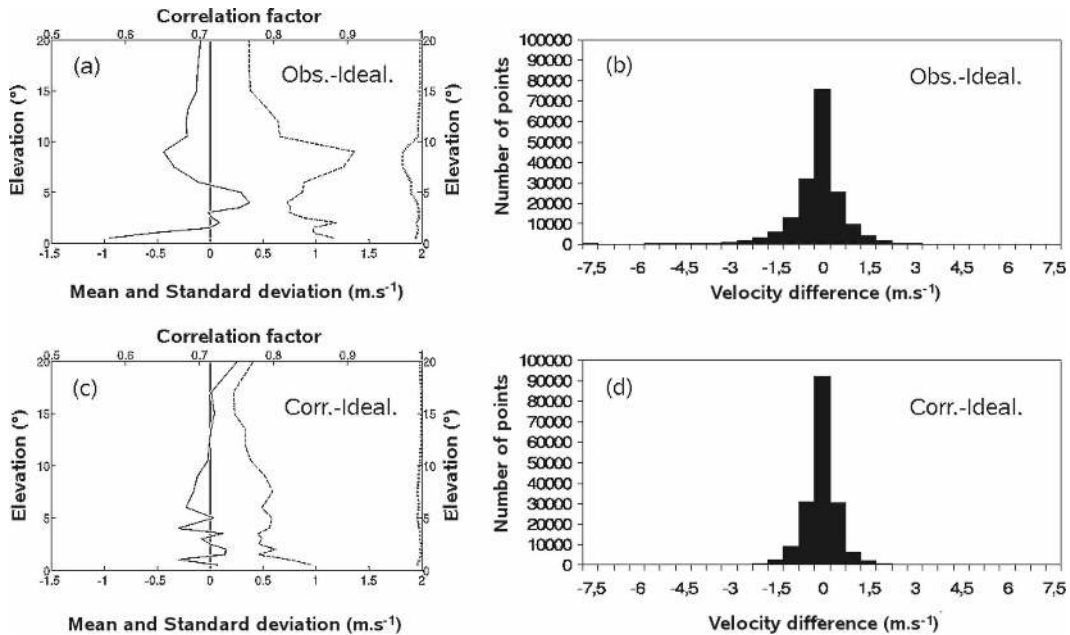
FIG. 6. (left) Elevation profiles of mean (solid line) and std dev (dashed line) of differences, and correlation factor (dotted line) between (a) observed and idealized bistatic apparent Doppler velocity and (c) sidelobe-corrected and idealized apparent Doppler velocity. (right) Histograms per class of 0.5 m s^{-1} of (b) observed minus idealized and (d) sidelobe-corrected minus idealized differences in Doppler velocity shown in (a) and (c), respectively.

illuminated ellipsoid surface can be concerned by more reflectivity and/or velocity variations than at a lower distance.

To quantify more precisely the improvement of the correction to the observed bistatic Doppler velocity, statistics of the observed minus idealized and corrected minus idealized differences (hereafter referred to as $O - I$ and $C - I$ differences, respectively) at each conical scan are estimated and plotted in Fig. 6. Figures 6a,b (Fig. 6c,d) represent the elevation profiles of the average and standard deviation of the $O - I$ ($C - I$) differences along with the correlation factor between observed (corrected) and idealized data, and the distribution of $O - I$ ($C - I$) differences per class of 0.5 m s^{-1}, respectively. These figures clearly demonstrate the significant reduction of the sidelobe contribution by the proposed method, which allows concentration of mean difference around zero (<0.3 m s^{-1} in magnitude) and standard deviation at a reasonable level of about 0.5 m s^{-1} throughout most of the scanned volume (Fig. 6c). This contrasts with the higher statistical values found in the $O - I$ differences (Fig. 6a), which could reach 1 and 1.3 m s^{-1}, respectively. The region of maximum standard deviation at 9° elevation angle is consistently associated with a decrease of the correlation factor. The correlation factor for the corrected dataset is roughly close to unity. Within the

whole volume, the distribution of the differences (Figs. 6b,d) is also consistent with the above discussion, with a larger dispersion of $O - I$ differences between −5.5 and 3.5 m s^{-1}, while the $C - I$ differences range within ±2 m s^{-1} with a higher peak level around zero. (Note the quasi-symmetrical character of this latter distribution around zero, suggesting that the sidelobe correction does not introduce additional bias.) As stated in section 2b, discrete representation of the correction method contributes to the difference between corrected and idealized Doppler velocity. Moreover, the largest standard deviation of the $C - I$ differences at the first radar elevation angle (0.5°) can be attributed to the fact that the correction method is limited to regions of available observations, implying the nonrepresentation of contributions at lower angles where either the main lobe or sidelobe hits the surface.

c. Corrected versus uncorrected retrieved 3D wind fields

The 3D wind fields from the combination of the observed, idealized, and corrected bistatic Doppler velocity datasets with the corresponding monostatic Doppler data have been processed according to the multiple-Doppler synthesis and continuity adjustment technique. The wind retrieval was performed over the Cartesian domain shown in Fig. 4, with a grid resolution
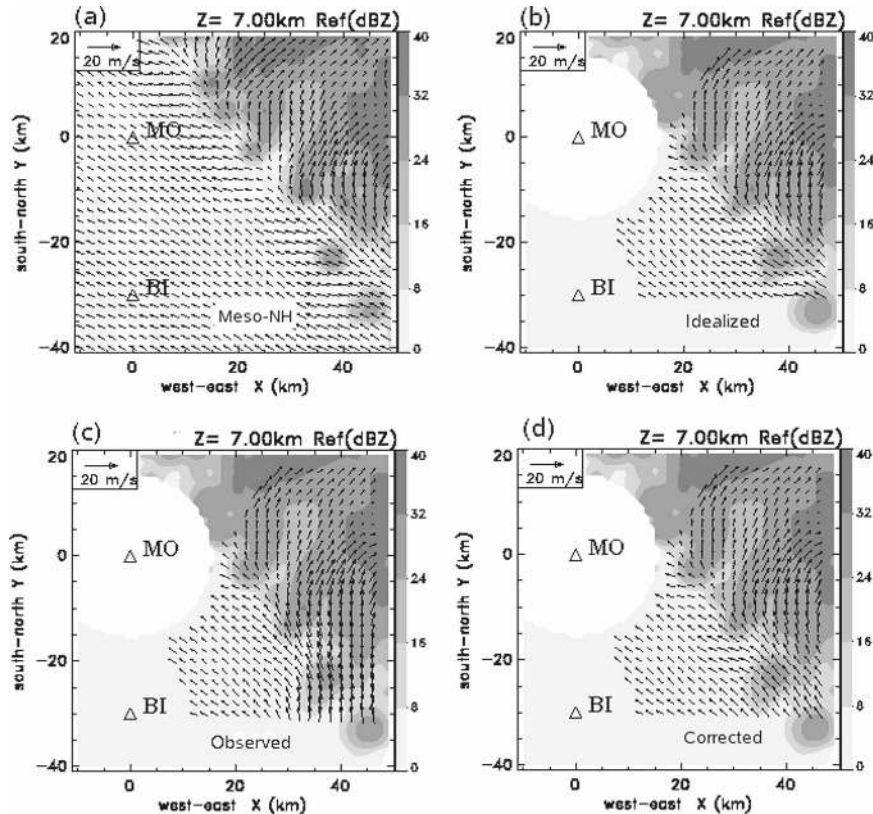
FIG. 7. Horizontal cross section of flow structure (vectors) and reflectivity (dBZ) pattern (grayscale) at 7-km altitude, as deduced from (a) numerical modeling and MUSCAT analysis of (b) idealized, (c) observed, and (d) sidelobe-corrected bistatic apparent Doppler velocity data, respectively, with monostatic Doppler data. Every other wind vector is plotted, and the scaling wind vector is indicated in the top left corner of each panel. MO and BI indicate the positions of the monostatic radar and bistatic receiver, respectively.

of 1 km in the horizontal and 0.5 km in the vertical. Details of the MUSCAT algorithm, initially developed for airborne Doppler data and later adapted to ground-based radar observations over flat or complex terrain, can be found in Bousquet and Chong (1998), Chong and Cosma (2000), and Chong and Bousquet (2001). The relationship between the wind components and the apparent bistatic Doppler velocity naturally takes into account the specific geometry of the bistatic measurements (Fig. 1). Because the 3D wind field issued from MUSCAT through a least squares analysis does not strictly satisfy the mass conservation equation, an a posteriori upward integration of this equation (with zero vertical velocity at the surface in the present study) is necessary and performed according to the method proposed by Georgis et al. (2000). This method aims at modifying the MUSCAT-derived horizontal wind components in such a way that they lead to vertical velocity with minimized horizontal gradients within the 3D volume and minimized magnitude at the upper boundary.

Figure 7 shows the wind vectors and reflectivity pattern at 7-km altitude, as simulated by the Meso-NH model (Fig. 7a), and issued from the analysis of idealized (Fig. 7b), observed (Fig. 7c), and corrected (Fig. 7d) data. An important point is the high quality of MUSCAT winds in the absence of sidelobe contamination (idealized case, Fig. 7b), which match well the simulated winds (Fig. 7a) in both intensity and direction. This allows us to compare directly the different retrieved wind fields (see below), which avoids considering the data-processing errors inherent to the data interpolation and filtering. As a consequence of sidelobe contamination, the observed winds exhibit a large region ($\approx 400 \mathrm{km}^2$) of overestimated intensity and false direction to the east of the bistatic receiver, ahead of the convective cells (Fig. 7c). At the leading edge of the squall-line system (around $x = 40 \mathrm{km}$ and $y = -25 \mathrm{km}$), the actual northwestward flow is observed as a northward inflow. By geometric construction from Figs. 7b,c, difference wind vectors are found to be mainly oriented
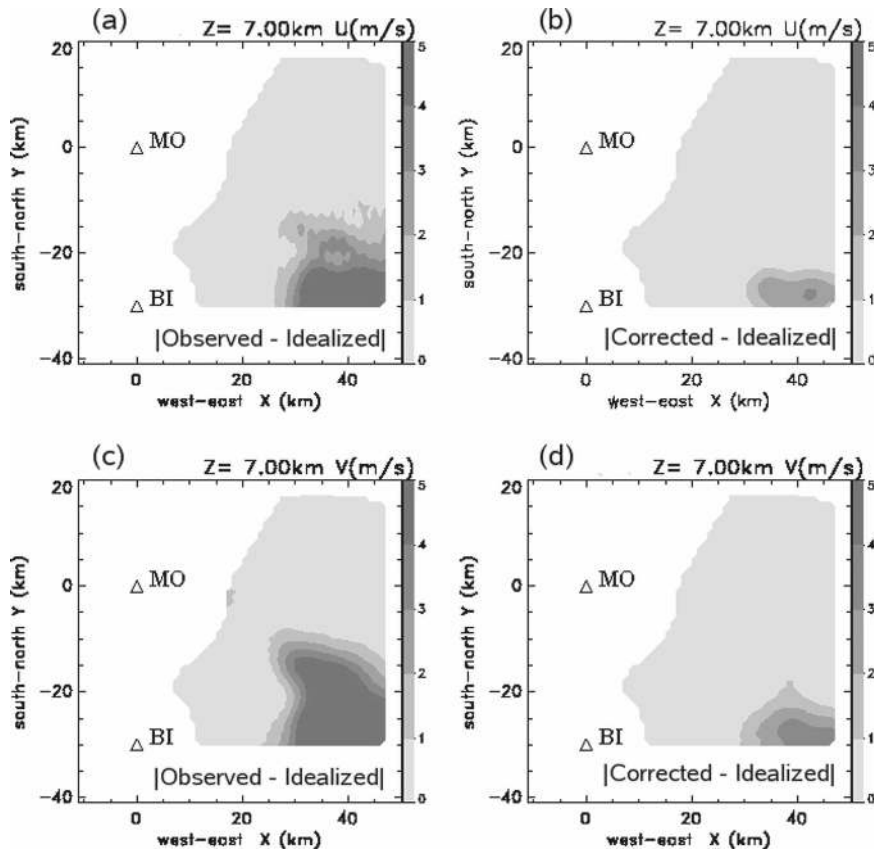
FIG. 8. Horizontal cross section of absolute differences in (a), (b) *u* and (c), (d) *v* wind components at 7-km altitude. The differences (left) between observed and idealized components and (right) between sidelobe-corrected and idealized components.

toward northeast, with major northward component. This biased flow no longer subsists with the corrected wind field (Fig. 7d), which remarkably resembles the idealized one. The associated $O - I$ and $C - I$ absolute differences in the wind component *u* (Figs. 8a,b, respectively) and *v* (Fig. 8c,d, respectively) indicate the dramatic extension of biased observed components that could result from the sidelobe contribution and its efficient diminution by the correction method (e.g., see the 3 m s^{-1} contour). It is interesting to note that the region of low observed differences (e.g., <1 m s^{-1}) supposed as sidelobe free, remains unchanged after correction, suggesting that no extra modification of the observed bistatic Doppler velocity is artificially introduced if not needed.

Statistics of the $O - I$ and $C - I$ differences at each level are shown in Figs. 9 (left and right, respectively), for horizontal wind component *u* (top, Figs. 9a,b) and *v* (middle, Figs. 9c,d) and vertical velocity *w* (bottom, Figs. 9e,f). An overall look at Fig. 9 gives an idea of how the correction method of sidelobe-contaminated bistatic Doppler velocity could yield a reliable 3D wind

field. Compared to the observed components, the corrected components have lower and stable residuals with the idealized ones throughout the depth of the retrieval domain. This improvement not only concerns the horizontal wind components but also the vertical velocity. The following comments arise from the examination of Figs. 9a,c,e. There is a region of predominant $O - I$ differences in *u* and *v* between 4- and 8-km altitude (Figs. 9a,c), associated with a region of potentially large gradients of reflectivity that favor sidelobe contamination (de Elía and Zawadzki 2000; Friedrich and Hagen 2004a). Both observed *u* and *v* are overestimated on average, with maximized standard deviations of the $O - I$ differences and rapid decorrelation, in a way consistent with the abovementioned northeastward orientation of the difference wind vectors of Figs. 7b,c, suggesting their major contribution. Larger differences in *v* are inherent to the dual-Doppler analysis, which is associated with an uncertainty nearly twice as large in the component parallel to the radar baseline as in the perpendicular component (Testud and Chong 1983). Finally, as side effects, statistics of the vertical velocity
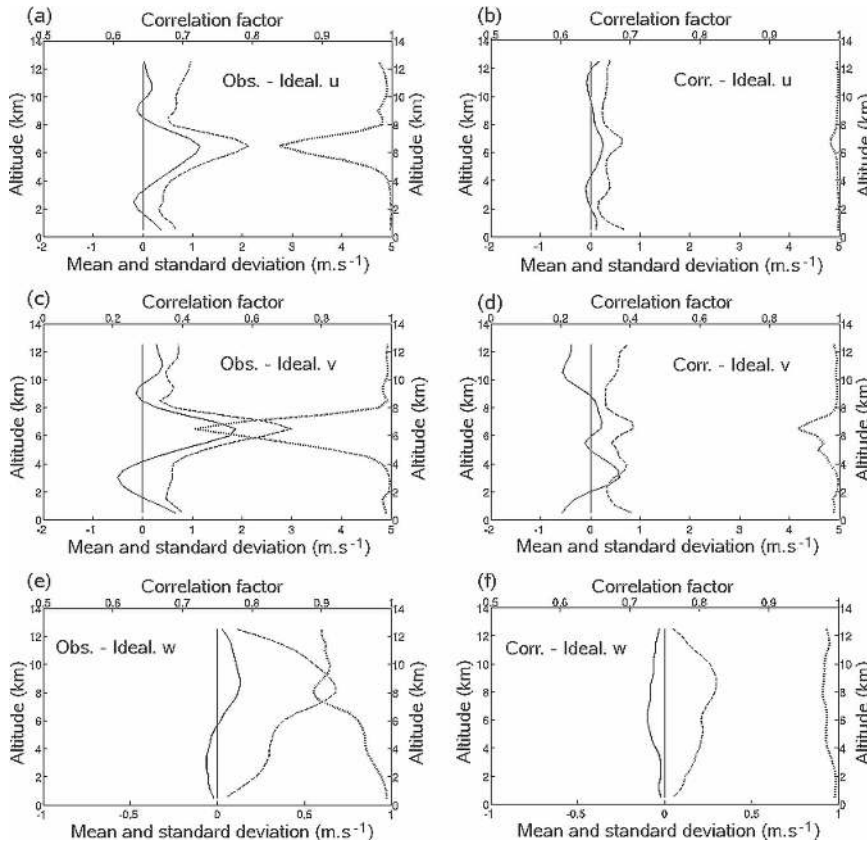
FIG. 9. Height profiles of mean (solid line) and std dev (dashed line) of differences, and correlation factor (dotted line) between (left) observed and idealized and (right) sidelobe-corrected and idealized wind components: (a), (b) *u* component, (c), (d) *v* component, and (e), (f) *w* vertical velocity. Note that the correlation factors for *u* and *w* are between 0.5 and 1, while those for *v* are between 0 and 1.

related to the horizontal wind components through the upward-integrated mass continuity equation tend to degrade upward, notably in the layer of largest $O - I$ differences in *u* and *v*. Maximum differences are obtained at the top of this layer (8 km) rather than the altitude (6.5 km) of maximum *u* and *v* differences, as a consequence of error accumulation in the upward integration process. Undoubtedly, 3D wind field analysis combining Doppler measurements from a bistatic Doppler radar network would greatly benefit from the use of a sidelobe correction to the measured bistatic Doppler velocity such as in the proposed method, as well avoiding discarding regions of potentially degraded data as in refining the description of the airflow structure.

4. Application to observed data

On 8 May 2000, the DLR bistatic Doppler radar network was operated during 1 h with the receiver in-

stalled at Lagerlechfeld, at 34 km to the west-northwest (290°) of the POLDIRAD monostatic Doppler radar located at Oberpfaffenhofen (southern Germany). The principal axis of the receiver was oriented at 142°, with an antenna aperture of 60° in the horizontal and 22° in the vertical. Data gathered at 1600 UTC are used in this study. They correspond to a case of nonaliased Doppler velocity, from both radar and receiver. Figure 10 shows the reflectivity pattern from POLDIRAD (Fig. 10a) and the corresponding apparent Doppler velocity as observed by the receiver (Fig. 10b), at an elevation angle of 3°. The edge of the bistatic data region (Fig. 10b) clearly delineates the horizontal aperture of the receiver (from Lagerlechfeld) and a portion of the farthest ellipsoid of constant delay time. Figure 10 indicates the presence of a precipitation cell (>24 dBZ) at the southern part of the bistatic observation domain, associated with a core of negative apparent Doppler velocity (<-5m s^{-1}). The POLDIRAD sampling was performed at eight successive elevation angles (i.e., 1°,
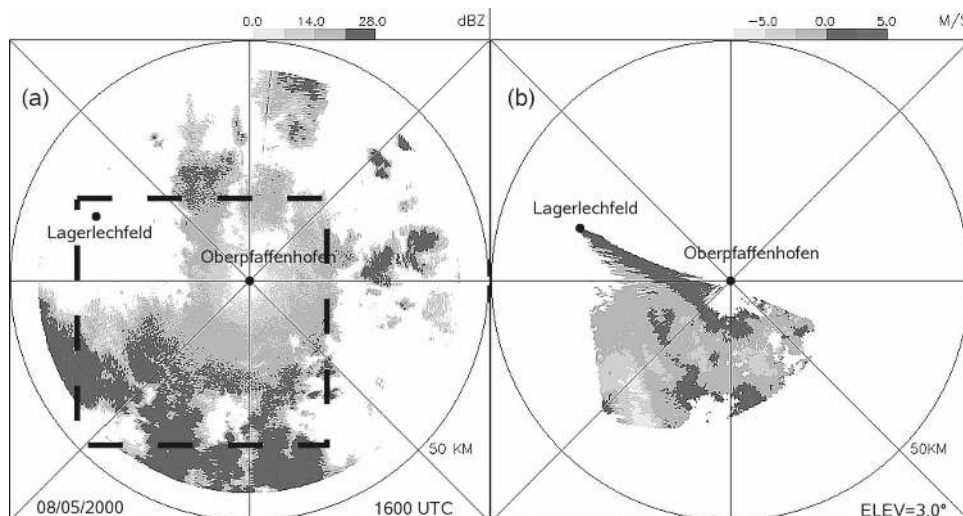
FIG. 10. PPI representation at 3° elevation, of (a) radar reflectivity (dB*Z*) from POLDIRAD (DLR) at Oberpfaffenhofen, and (b) bistatic apparent Doppler velocity (m s^{-1}) measured at Lagerlechfeld to the northwest of POLDIRAD, 1600 UTC 8 May 2000. Dashed square outlines the domain of wind analysis.

2°, 3°, 5°, 7°, 10°, 14°, and 20°, respectively), with an azimuthal increment of 0.63°, and over a range of 45 km with a range gate spacing of 150 m. At the receiver, 126 range gates were sampled with a delay time increment of 1.25 μs. The sidelobe-correction method has been applied to the observed bistatic apparent Doppler velocity, with the discretized radar and receiver antenna gain pattern as described in section 3a. Finally, 3D wind field analysis from either observed or corrected Doppler measurements has been performed in a Cartesian frame of 50 km × 50 km, centered at (−10 km, −10 km) from POLDIRAD, with a grid resolution of 0.5 km in the horizontal and 0.2 km in the vertical.

A comparison of the corrected and observed wind field is shown in Fig. 11. The corrected flow structure and precipitation pattern at 0.2-km altitude (above ground level) is presented in Fig. 11a, while Fig. 11b is a plot of the $C - O$ difference wind vectors. These are the correction vectors that should be added to the observed (sidelobe contaminated) wind vectors to obtain the corrected wind vectors. In particular, an eastward orientation of these $C - O$ wind vectors is found in a region of northwesterly low-level flow at the southern edge of the observed domain. Although these corrections appear quite small (<1–2 m s^{-1}), they are consistent with the reflectivity pattern. Indeed, the major corrections to the south occur in a region where a reflectivity gradient may have influenced the apparent bistatic Doppler measurements. As long as the corrected wind field may represent the actual wind field, this region can be viewed as of the highest improve-

ment. It is also interesting to analyze the importance of the improvement in the observed bistatic Doppler velocity. Figure 12 represents the elevation profiles of average and standard deviation of the $C - O$ differences. The correlation factor between observed and corrected bistatic Doppler data is also reported. On average, the sidelobe correction does not affect greatly the observations because the magnitude of the mean correction is below 0.2 m s^{-1}. However, the relatively large dispersion (>0.75 m s^{-1}) of the differences at low and high elevation angles suggests that punctual improvement may have been realized, and hence the lower the correlation factor, the higher the correction/improvement.

Figures 13a–d present the statistics of the $C - O$ differences for the Cartesian wind components u and v, respectively. Because the vertical component w results from the estimation of u and v, the differences for this parameter will not be discussed here. Height profiles on the left-hand side are obtained within the full domain of interest, while those on the right-hand side concern a limited domain containing the major correction as found in Fig. 11b and defined as $x = [−20, 10]$ km and $y = [−30, –20]$ km. With respect to the wind analysis domain (Fig. 13a,c), the mean differences in u and v are close to zero, suggesting that sidelobe contamination could not generate large wind bias as in the simulated case. However, their close standard deviation between 0.5 and 1.0 m s^{-1} indicates that both components are improved by the correction of the bistatic Doppler measurements, as also measured by the deviation of the

FIG. 12. Elevation profiles of mean (solid line) and std dev (dashed line) of differences, and correlation factor (dotted line) between sidelobe-corrected and observed bistatic apparent Doppler velocity.

mosphere, mainly due to the Doppler velocity correction at the first elevation angle (Fig. 12). It is probable that surface ground-clutter contamination may have contributed to the large difference at lower altitudes in addition to large reflectivity difference.

5. Conclusions

This paper analyzes a solution to the problem of sidelobe contamination of bistatic apparent Doppler velocity measurements involved in a bistatic Doppler radar network. So far in the context of 3D wind field analysis, by combining a traditional Doppler radar with one or more bistatic receivers, identification and hence removal of regions of high degrees of contamination were necessarily crucial steps to obtaining reliable wind fields. Several methods were then proposed, using the monostatic radar reflectivity assumed to be noncontaminated by sidelobes either to detect echo regions with large gradients generally observed to be associated with sidelobe effects or to evaluate the degree of contamination by modeling and comparing the sidelobe and total powers that reach the receiver, for example. The wind field analysis will truly benefit from a systematic elimination of such regions of potentially degraded bistatic apparent Doppler velocity, at the cost of considerably reducing the volume that is visible to each receiver and hence the volume description of the airflow structure.

In this study, an alternative has been examined to the forced rejection of bistatic Doppler data suspected to be contaminated by sidelobe echoes, on the basis of restoring the nonmeasured actual (i.e., noncontaminated) bistatic Doppler velocity from both monostatic radar and bistatic receiver measurements. The correc-
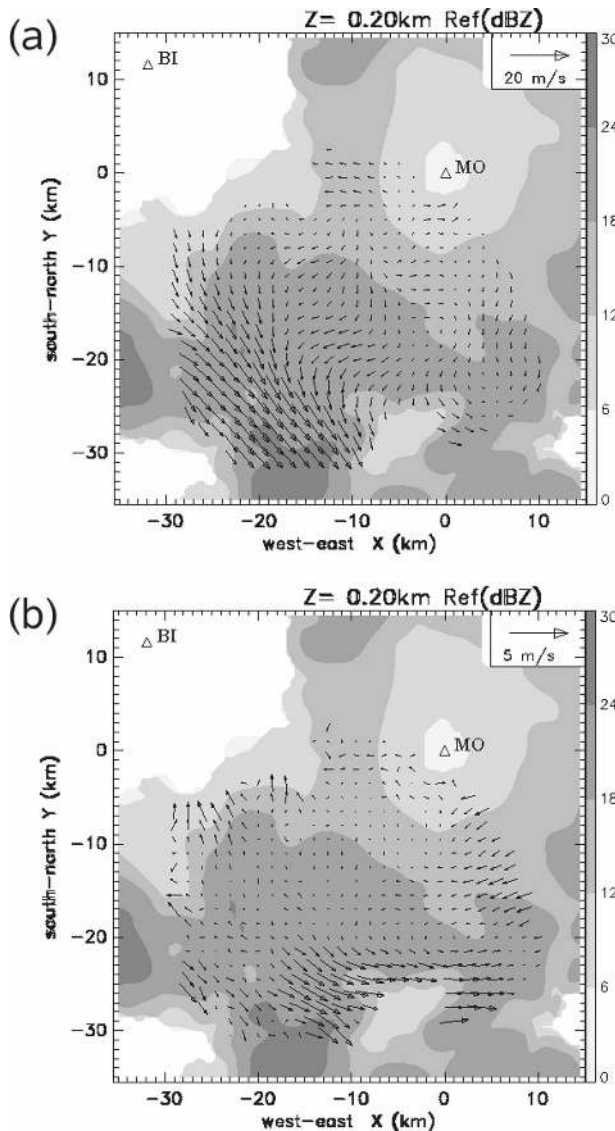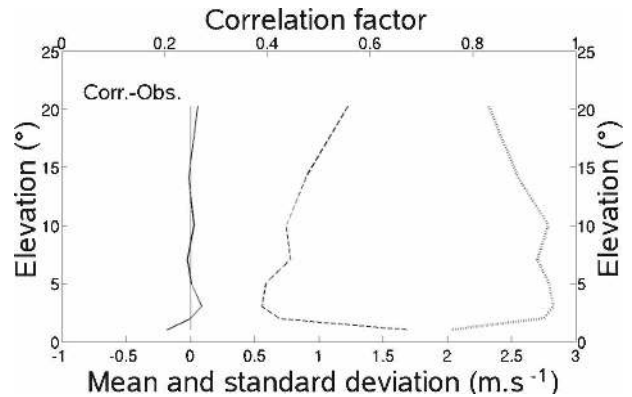
FIG. 11. Horizontal cross section of MUSCAT-derived wind (vectors) and reflectivity field (grayscale) at 0.2-km altitude: (a) sidelobe-corrected wind structure and (b) corrected minus observed wind field. The scaling vector is indicated at the top right corner of each panel. MO and BI represent the location of the monostatic radar and bistatic receiver.

correlation factor from unity. The height variations of the correlation factor greatly resemble the mirror image of the standard deviation variations. Within the limited box (Figs. 13b,d), the height profiles of the $(C - O)$ u and v differences clearly show that the major improvement is accomplished for the u component. Globally, the corrections for u are more than twice those for v, consistently with the mostly west–east orientation of the radar baseline along which wind components have larger uncertainty (Testud and Chong 1983). Note also that they are concentrated in the lower part of the at-
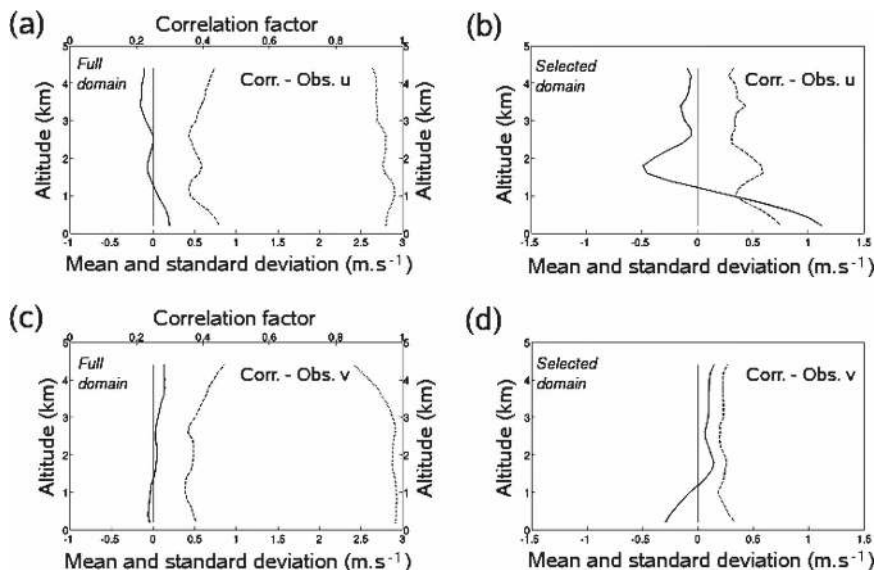
FIG. 13. Height profiles of mean (solid line) and std dev (dashed line) of differences between sidelobe-corrected and observed horizontal wind components, within the (left) whole domain and (right) a limited (see text) domain of maximized differences: (a), (b) u component and (c), (d) v component. The correlation factors for u and v within the whole domain are also plotted in (a) and (c), respectively.

tion approach has been established on a modeled expression of the observed bistatic apparent Doppler velocity, which is defined as the reflectivity-weighted average of actual Doppler velocity of particles within individual volume samples. This expression involves the antenna gain pattern of both transmitting and receiving radars. It was shown that the searched actual Doppler velocity can be a solution of an underdetermined inverse problem that can be handled as a constrained (regularization) linear inversion problem. A variational least squares analysis method has been developed on discrete points of bistatic observations at a constant time delay lying on an ellipsoid surface, with a regularization constraint based on the second derivatives and acting as a low-pass filter.

To analyze the performances of the proposed sidelobe-correction method, an application to simulated radar observations involving one remote receiver was carried out. An example of an application to experimental data collected by DLR bistatic Doppler radar network within a moderate precipitation system observed on 8 May 2000 in Germany was also presented. Characteristics of this radar network were used to simulate pseudo-Doppler observations from a modeled tropical squall-line system. In particular, an idealized but impracticable dataset was generated, consisting of fully sidelobe-free bistatic apparent Doppler velocity. This permitted quantification of the effective improvement of the correction method on the bistatic Doppler veloc-

ity and hence the retrieved 3D wind field, through a comparative study. Statistics of the differences between observed and idealized velocity structure (including Doppler velocity and deduced Cartesian wind components) on the one hand, and corrected and idealized velocity structure on the other hand, clearly showed the very low level of the corrected minus idealized differences (mean and standard deviation) against the significantly high level of the observed minus idealized differences. As previously observed, maximized severe (in the simulated case) to low (in the experimental application) correction occurred in regions of potentially high gradients of reflectivity. It was also found that regions of low observed minus idealized differences remained unchanged after correction, which means that the sidelobe-correction method only acts on needed regions and does not introduce any artificial modification. Finally, the proposed sidelobe correction offers a real opportunity to take advantage of the full coverage of bistatic Doppler measurements (say, without rejection of sidelobe-contaminated data) from a bistatic Doppler radar network, dedicated to the description of the three-dimensional airflow structure.

REFERENCES

Bousquet, O., and M. Chong, 1998: A Multiple-Doppler Synthesis and Continuity Adjustment Technique (MUSCAT) to recover wind components from Doppler radar measurements. *J. Atmos. Oceanic Technol.,* **15,** 343–359.

Chong, M., and S. Cosma, 2000: A formulation of the continuity equation of MUSCAT for either flat or complex terrain. *J. Atmos. Oceanic Technol.,* **17,** 1556–1565.

——, and O. Bousquet, 2001: On the application of MUSCAT to a ground-based dual-Doppler radar system. *Meteor. Atmos. Phys.,* **78,** 133–139.

de Elía, R., and I. Zawadzki, 2000: Sidelobe contamination in bistatic radars. *J. Atmos. Oceanic Technol.,* **17,** 1313–1329.

Doviak, R. J., and D. S. Zrnić, 1993: *Doppler Radar and Weather Observations.* Academic Press, 562 pp.

Friedrich, K., 2002: Determination of three-dimensional wind-vector fields using a bistatic Doppler radar network. Ph.D. thesis, Fakultaet fuer Physik, Ludwig-Maximilians-Universitaet Muenchen, 135 pp.

——, and M. Hagen, 2004a: Wind synthesis and quality control of multiple-Doppler-derived horizontal wind fields. *J. Appl. Meteor.,* **43,** 38–57.

——, and ——, 2004b: Evaluation of wind vectors measured by a bistatic Doppler radar network. *J. Atmos. Oceanic Technol.,* **21,** 1840–1854.

Georgis, J.-F., F. Roux, and P. H. Hildebrand, 2000: Observation of precipitating systems over complex orography with meteorological Doppler radars: A feasibility study. *Meteor. Atmos. Phys.,* **72,** 185–202.

Lafore, J.-P., and Coauthors, 1998: The Meso-NH atmospheric simulation system. Part I: Adiabatic formulation and control simulations. *Ann. Geophys.,* **16,** 90–109.

Press, W. H., S. A. Teukolsky, W. T. Vetterling, and B. P. Flannery, 1992: *Numerical Recipes in C: The Art of Scientific Computing.* 2nd ed. Cambridge University Press, 994 pp.

Protat, A., and I. Zawadzki, 1999: A variational method for real-time retrieval of three-dimensional wind field from multiple-Doppler bistatic radar network data. *J. Atmos. Oceanic Technol.,* **16,** 432–449.

Satoh, S., and J. Wurman, 2003: Accuracy of wind field observed by a bistatic Doppler radar network. *J. Atmos. Oceanic Technol.,* **20,** 1077–1091.

Schroth, A. C., M. S. Chandra, and P. Meischner, 1988: A C-band coherent polarimetric radar for propagation and cloud physics research. *J. Atmos. Oceanic Technol.,* **5,** 803–822.

Takaya, Y., and M. Nakazato, 2002: Error estimation of the synthesized two-dimensional horizontal velocity in a bistatic Doppler radar system. *J. Atmos. Oceanic Technol.,* **19,** 74–79.

Testud, J., and M. Chong, 1983: Three-dimensional wind field analysis from dual-Doppler radar data. Part I: Filtering, interpolating, and differentiating the raw data. *J. Climate Appl. Meteor.,* **22,** 1204–1215.

Wurman, J., 1994: Vector winds from a single-transmitter bistatic dual-Doppler radar network. *Bull. Amer. Meteor. Soc.,* **75,** 983–994.

——, S. Heckman, and D. Boccippio, 1993: A bistatic multiple-Doppler network. *J. Appl. Meteor.,* **32,** 1802–1814.